Int. J. Electron. Commun. (AEÜ) 218 (2027) 156647

Contents lists available at ScienceDirect

Int. J. Electron. Commun. (AEÜ)

journal homepage: www.elsevier.com/locate/aeue

Regular paper

# Fluid-antenna-aided SWIPT UAV–NOMA relaying: Analysis and deployment

Khalid Yahya [a,b,*], Mahmoud Aldababsa [c], Hamidullah Riaz [d]

[a] Institute of Research and Development, Duy Tan University, Da Nang, Viet Nam
[b] School of Engineering & Technology, Duy Tan University, Da Nang, Viet Nam
[c] Department of Electrical and Electronics Engineering, Istanbul Nisantasi University, Istanbul 34481742, Turkey
[d] Department of Electrical and Electronics Engineering, Faculty of Engineering and Architecture, Istanbul Gelisim University, Istanbul, 34310, Turkey

ARTICLE INFO

*Keywords:*
Amplify-and-forward relaying
Fluid antenna systems
Nonorthogonal multiple access
Outage probability
Simultaneous wireless information and power transfer
Unmanned aerial vehicle deployment

ABSTRACT

This paper develops an outage-analysis and deployment framework for a power-splitting simultaneous wireless information and power transfer (SWIPT)-enabled unmanned aerial vehicle (UAV) relay serving multiple fluid-antenna users through half-duplex variable-gain amplify-and-forward nonorthogonal multiple access (NOMA) relaying. The instantaneous relay gain is derived from the harvested-energy constraint. Under the exact relay gain, each layer-decoding condition is transformed into a selected-gain-dependent threshold on the base-station–UAV channel, yielding an exact one-dimensional outage integral for an arbitrary distribution of the selected fluid-antenna gain. A relay-input signal-to-noise ratio (SNR) approximation then produces tractable correlated-port outage representations and an independent-port closed-form expression. Spatial dependence is modeled using a Gaussian copula calibrated to the power-gain correlation induced by a physical complex-channel model. The asymptotic analysis establishes diversity order one under a finite inverse-moment condition and separately characterizes the logarithmically modified single-port behavior. For deployment, a globally optimal bounded weighted-centroid benchmark is derived for a convex geometric surrogate, and a data-driven initializer validated using the exact outage objective is developed. The baseline derivations assume Rayleigh fading, linear energy harvesting, perfect channel state information, ideal successive interference cancellation, and a predetermined decoding order. Their robustness is numerically assessed under Rician fading, a sensitivity-and-saturation nonlinear energy-harvesting model, aged port-selection channel state information, residual successive interference cancellation, and instantaneous order adaptation. The proposed placement initializer is also compared with random-forest and multilayer-perceptron alternatives.

## 1. Introduction

The rapid expansion of Internet of Things (IoT) applications is increasing the demand for wireless networks that can support a large number of devices with diverse reliability, coverage, and energy requirements [1]. In many practical environments, however, terrestrial infrastructure may be unavailable, damaged, congested, or unable to provide satisfactory connectivity to remote and obstructed areas [2]. Unmanned aerial vehicles (UAVs) have therefore emerged as flexible airborne communication platforms that can rapidly extend coverage, establish temporary links, and improve service availability for distributed IoT devices [3]. Their adjustable positions and favorable propagation conditions make them particularly attractive for emergency communications, environmental monitoring, industrial sensing, intelligent transportation, and smart-city applications [4].

Despite these advantages, the operation of UAV-assisted networks is constrained by limited onboard energy. Communication, signal processing, propulsion, and hovering consume a considerable amount of power, which restricts the duration for which a UAV can support ground devices [5]. Simultaneous wireless information and power transfer (SWIPT) provides a promising approach for reducing the dependence of airborne relays on conventional energy sources [6]. Through power splitting, a portion of the received radio-frequency (RF) signal can be used for energy harvesting (EH), while the remaining portion is reserved for information processing. The harvested energy can subsequently support the forwarding operation of the UAV relay. Nevertheless, the power-splitting ratio must be carefully selected because increasing the harvested energy reduces the fraction of the received signal available for information processing. This coupling creates an important reliability–energy tradeoff in UAV-assisted communications.

At the same time, massive IoT connectivity requires multiple devices to share limited radio resources efficiently. Power-domain nonorthogonal multiple access (NOMA) addresses this requirement by allowing several users to be served over the same time and frequency resources

* Corresponding author.
*E-mail addresses:* halityahya@duytan.edu.vn (K. Yahya), mahmoud.aldababsa@nisantasi.edu.tr (M. Aldababsa), hriaz@gelisim.edu.tr (H. Riaz).

https://doi.org/10.1016/j.aeue.2026.156647
Received 27 July 2026; Accepted 28 September 2026
Available online 6 October 2026
1434-8411/© 2026 Elsevier GmbH. All rights are reserved, including those for text and data mining, AI training, and similar technologies.

through superposition transmission and user-dependent power allocation [7–9]. Compared with orthogonal access, NOMA can improve connectivity and spectral-resource utilization, particularly when users experience different channel conditions. In a UAV-assisted relay network, however, the performance of NOMA users depends jointly on the first-hop channel, the energy harvested at the UAV, the second-hop user channels, the adopted power allocation, and the target transmission rates. The random interaction among these components makes the end-to-end reliability analysis substantially more involved than that of a conventional single-hop NOMA system.

Fluid antenna systems (FASs) offer an additional means of improving reception at energy-constrained IoT devices [10]. Unlike conventional multiple-antenna receivers that require several simultaneously active RF chains, an FAS can select an effective antenna position from a set of candidate ports distributed over a compact region. By activating the port with the strongest instantaneous channel gain, the receiver can exploit spatial channel variations with limited hardware complexity. The achievable selection benefit, however, strongly depends on the statistical dependence among the candidate ports. Assuming independent ports may overestimate the performance when the antenna aperture is small, whereas a correlated-port model provides a more realistic description of practical FAS implementations [11].

### 1.1. Related work

Research related to the considered system has progressed along several directions. In UAV-assisted NOMA relaying, Hoang et al. [12] analyzed the outage performance of a multi-antenna mobile UAV relay serving NOMA users over Nakagami-$m$ fading channels. Their results demonstrated the effects of the UAV location, propagation conditions, antenna configuration, and power allocation on user reliability. However, the UAV forwarding operation was not powered through SWIPT, and the ground users were not equipped with position-reconfigurable antennas. Wireless-powered UAV relaying has also received considerable attention. Kim et al. [6] investigated a power-splitting SWIPT-enabled UAV relay and optimized the power-splitting and time-allocation parameters to improve the outage performance of a blocked source–destination link. Similarly, Yin et al. [13] considered a wirelessly powered UAV relay and jointly optimized its power profile, power-splitting profile, and trajectory for end-to-end throughput maximization. Perera et al. [14] investigated a full-duplex UAV-assisted cooperative communication system over Nakagami-$m$ fading, in which the UAV's forwarding operation was powered by energy harvested from both the source signal and self-interference through a power-splitting SWIPT protocol. They derived a closed-form outage expression and optimized the power-splitting factor using the Karush–Kuhn–Tucker conditions. Wang et al. [15] investigated secure communications through an energy-constrained amplify-and-forward (AF) UAV relay in the presence of multiple eavesdroppers with imperfect location information. The UAV employed power splitting for simultaneous information reception and EH and time switching for information forwarding, while a full-duplex destination transmitted artificial noise to jam the eavesdroppers. The UAV position, power-splitting and time-switching ratios, and artificial-noise power were jointly optimized to maximize the worst-case minimum secrecy rate. However, their framework did not consider NOMA transmission, fluid-antenna users, correlated port selection, or user-outage-oriented UAV deployment. Mamaghani and Hong [16] investigated secure SWIPT-enabled communications employing two cooperative UAVs, where one UAV transmitted confidential information and the other provided cooperative jamming and additional RF energy to a power-splitting ground receiver. Under partial knowledge of the eavesdropper's location, they jointly optimized the UAV trajectories, transmit-power profiles, and receiver power-splitting ratio to maximize the average secrecy rate. However, the UAVs acted as an aerial transmitter and jammer rather than a SWIPT-powered AF relay, and the framework did not consider NOMA, fluid-antenna port selection, or outage-oriented multiuser deployment. These studies established the benefits of SWIPT for UAV relaying, but they primarily considered single-pair communication and did not address multiuser NOMA transmission or FAS-assisted reception. The integration of EH and UAV-assisted NOMA was examined in [17], where a wirelessly powered UAV employed AF or decode-and-forward relaying to serve grouped NOMA users. Closed-form outage-probability and ergodic-capacity expressions were developed for both relaying protocols. More recently, Thapliyal et al. [18] investigated an EH-enabled decode-and-forward UAV-relay NOMA network under finite-blocklength transmission. Using stochastic geometry, they analyzed the outage probabilities of randomly paired near and far users in the presence of intercell interference, while accounting for power splitting, decoding-energy consumption, and both linear and nonlinear EH models. Boshkovska et al. [19] proposed a measurement-validated nonlinear RF-EH model that captures input-power-dependent conversion efficiency and saturation. They demonstrated that resource allocation based on the conventional constant-efficiency linear model can result in substantial performance loss when applied to practical harvesting circuits. Taken together, these studies provide complementary insights into EH-enabled UAV–NOMA relaying and practical nonlinear energy conversion. Nevertheless, they employ conventional fixed-position antenna architectures and do not characterize how FAS port selection and intra-aperture spatial correlation interact with SWIPT-powered variable-gain AF–NOMA relaying. In parallel, several works have investigated the statistical performance of FAS-assisted communication. The fundamental ability of an FAS receiver to select a favorable port from a compact spatial region was established in [10]. The outage performance of $N$-port FAS reception over spatially correlated Nakagami-$m$ fading was investigated in [20], where the joint statistics of the candidate-port gains were derived to explicitly account for spatial dependence in the evaluation of port-selection performance. The outage behavior of two-user fluid antenna multiple access (FAMA) was revisited in [21] by explicitly characterizing the joint spatial correlation among the candidate ports. The study derived a closed-form outage lower bound and tractable approximations, showing that increasing the number of ports reduces the outage probability but produces an error floor unless the physical antenna aperture is also enlarged. More closely related to the present setting, Abdou et al. [22] considered a UAV relay-aided FAS–NOMA system and jointly optimized the active port, power allocation, and UAV altitude for sum-rate maximization. Ghadi et al. [23] analyzed the outage probability of a decode-and-forward UAV relay serving FAS users through rate-splitting multiple access. Xu et al. [24] studied AF/DF relaying when the fluid antenna is carried by an autonomous aerial vehicle and used a Gaussian copula for weak-user outage analysis. These studies establish the relevance of combining aerial relays, flexible antennas, and nonorthogonal signaling, but they do not address a SWIPT-powered variable-gain AF relay whose forwarding power is coupled to the instantaneous first-hop channel and whose ground users perform FAS port selection. UAV positioning and trajectory design have likewise been widely investigated as mechanisms for improving coverage, throughput, and energy efficiency [4,13]. Most communication-aware placement approaches, however, require repeated nonlinear optimization as the user geometry or service requirements change.

### 1.2. Research gap and motivation

The closest available UAV–FAS studies do not jointly capture four features of the considered link: instantaneous SWIPT-powered variable-gain AF forwarding, layered NOMA decoding, selection over dependent FAS ports, and outage-aware horizontal deployment. Their combination is not a direct extension of a single-hop result because the first-hop gain determines both the information delivered to the relay and the energy available for forwarding. The selected second-hop gain then enters a

layer-dependent quadratic decoding condition under the exact relay model.

A second difficulty concerns spatial dependence. The Jakes coefficient describes the correlation of complex channel samples, whereas outage depends on channel power gains and on the maximum across ports. Directly using the complex correlation as the latent Gaussian-copula correlation is therefore generally inconsistent. A calibrated copula can provide a tractable surrogate, but its approximation error must be reported rather than treating it as an exact physical distribution.

Finally, geometric centroids, approximate-outage optimization, and data-driven placement should not be conflated. A useful deployment framework must identify which objective is optimized online and must evaluate the resulting coordinates under the exact variable-gain model. These observations motivate the exact and approximate analyses, calibrated dependence model, and exact-objective placement validation developed below.

### 1.3. Main contributions

The main contributions of this paper are summarized as follows:

- We develop a unified reliability and deployment framework for a power-splitting SWIPT-enabled UAV that serves multiple fluid-antenna users through half-duplex variable-gain AF-NOMA relaying. Unlike fixed-gain models, the instantaneous relay gain is derived directly from the harvested-energy constraint.
- For the exact variable relay gain, the decoding requirements of all relevant NOMA layers are reduced to a single user-dependent threshold on the BS–UAV channel. This transformation leads to an exact one-dimensional outage integral that remains valid for an arbitrary distribution of the selected fluid-antenna channel gain.
- To obtain more computationally efficient expressions, we introduce a relay-input-SNR-based approximation. Based on this approximation, two one-dimensional outage representations are derived for spatially correlated FAS ports, while a closed-form expression involving the modified Bessel function of the second kind is obtained for independent ports.
- We construct a Gaussian-copula model for the correlated FAS power gains. Instead of directly using the Jakes channel-correlation coefficient as the copula parameter, the latent copula correlation is calibrated to reproduce the power-gain correlation generated by the underlying complex-channel model. The accuracy of the resulting surrogate model is verified through numerical comparisons.
- We characterize the high-SNR outage behavior of the considered system. The analysis proves that the overall diversity order is one whenever the required inverse moment of the selected FAS gain is finite. The distinct logarithmically modified asymptotic behavior of the single-port case is also derived separately.
- For UAV deployment, we derive a globally optimal bounded weighted-centroid solution that provides a simple geometric placement benchmark. For dynamic network configurations, we further develop a data-driven placement method in which a validation-selected nearest-neighbor predictor generates an initial UAV position, followed by a low-complexity local outage search.
- The proposed placement strategies are evaluated using both the approximate and exact outage objectives. This comparison separates the computational model used for efficient UAV positioning from the exact reliability model used for final performance assessment.
- Finally, to test whether the baseline conclusions survive practical modeling changes, we add controlled robustness experiments for Rician LoS components, nonlinear sensitivity-and-saturation harvesting, aged port-selection channel state information (CSI), residual successive interference cancellation (SIC), and instantaneous NOMA ordering. We further compare the nearest-neighbor initializer with random-forest and multilayer-perceptron regressors under an identical local-refinement and exact-objective evaluation protocol.

## 2. System model

### 2.1. Network architecture and propagation model

Consider a downlink UAV-assisted NOMA network composed of one single-antenna BS, one single-antenna UAV relay, and $K$ ground users. The direct BS–user links are assumed to be unavailable because of severe blockage and shadowing. Hence, every message transmitted by the BS reaches the users through the UAV. Let $\boldsymbol{q}_{BS} = (x_{BS}, y_{BS}, 0)$, $\boldsymbol{q}_{UAV} = (x_{UAV}, y_{UAV}, H)$, and $\boldsymbol{q}_k = (x_k, y_k, 0)$ denote the locations of the BS, UAV, and $k$th user, respectively. The corresponding link lengths are $d_{BU} = \|\boldsymbol{q}_{UAV} - \boldsymbol{q}_{BS}\| = \sqrt{(x_{UAV} - x_{BS})^2 + (y_{UAV} - y_{BS})^2 + H^2}$, and $d_{Uk} = \|\boldsymbol{q}_{UAV} - \boldsymbol{q}_k\| = \sqrt{(x_{UAV} - x_k)^2 + (y_{UAV} - y_k)^2 + H^2}$.

The UAV operates according to a half-duplex AF protocol. One transmission block of duration $T$ is divided into two equal phases. During the first phase, the BS transmits and the UAV simultaneously performs EH and information processing (IP) by means of a power-splitting (PS) receiver. During the second phase, the UAV forwards an amplified version of its received signal. The BS–UAV channel is denoted by $h_{BU}$ and follows $h_{BU} \sim \mathcal{CN}(0, \Omega_{BU})$, and $\Omega_{BU} = \beta_0 d_{BU}^{-\nu_{BU}}$, where $\beta_0$ is the average channel power gain at a reference distance of 1 m and $\nu_{BU}$ is the path-loss exponent. Define $Z \triangleq |h_{BU}|^2$ and since $h_{BU}$ is circularly symmetric complex Gaussian, $Z$ is exponentially distributed with $f_Z(z) = \frac{1}{\Omega_{BU}} \exp\left(-\frac{z}{\Omega_{BU}}\right)$, and $F_Z(z) = 1 - \exp\left(-\frac{z}{\Omega_{BU}}\right)$.[1]

### 2.2. First transmission phase: NOMA signaling and SWIPT reception

The BS superposes the messages of all users in the power domain. Its transmitted signal is

$$x_B = \sum_{i=1}^{K} \sqrt{\alpha_i P_B}\, s_i, \tag{1}$$

where $P_B$ is the BS transmit power, $\mathbb{E}\{|s_i|^2\} = 1$, and $\alpha_i$ is the power fraction assigned to $i$th user. The allocation coefficients satisfy $\alpha_i > 0$, and $\sum_{i=1}^{K} \alpha_i = 1$. A fixed NOMA decoding order is adopted such that 1st user is assigned the highest power and $K$th user the lowest power, i.e., $\alpha_1 > \alpha_2 > \cdots > \alpha_K$. The signal received by the UAV is

$$y_U = h_{BU} x_B + n_U, \tag{2}$$

where $n_U \sim \mathcal{CN}(0, \sigma_U^2)$. A fraction $\rho$, $0 < \rho < 1$, of the received RF power is directed to the EH circuit, whereas the remaining fraction $1 - \rho$ is used for IP. Under an ideal linear EH model with no storage loss, saturation, or peak relay-power limit, and ignoring the negligible energy contained in receiver noise, the energy harvested during the first phase is $E_H = \eta \rho P_B Z \frac{T}{2}$, where $0 < \eta \leq 1$ is the RF-to-DC conversion efficiency. Because the harvested energy is used over the second interval of duration $T/2$, the instantaneous UAV transmit-power budget becomes $P_U = \frac{E_H}{T/2} = \eta \rho P_B Z$. The signal delivered to the IP branch is

$$y_{\mathrm{IP}} = \sqrt{1 - \rho}\left(h_{BU} x_B + n_U\right). \tag{3}$$

and its average power is

$$P_{\mathrm{IP}} \triangleq \mathbb{E}\left\{|y_{\mathrm{IP}}|^2\right\} = (1 - \rho)\mathbb{E}\left\{\left|h_{BU} x_B + n_U\right|^2\right\}$$

[1] The first and second hops are statistically independent, and the user channel vectors are mutually independent. The closed-form baseline assumes perfect channel knowledge for port selection, ideal cancellation of decoded layers, and a predetermined service order kept fixed during placement. These assumptions make the outage event analytically inspectable; Section 2.5 defines the Rician, nonlinear-EH, aged-CSI, residual-SIC, and adaptive-order models used to quantify their impact. Rayleigh fading is therefore retained as the analytical baseline rather than asserted as a universal aerial-channel law.

$$= (1-\rho)\left(|h_{BU}|^2\mathbb{E}\{|x_B|^2\} + \mathbb{E}\{|n_U|^2\}\right)$$
$$= (1-\rho)(P_B Z + \sigma_U^2), \tag{4}$$

where the cross term vanishes because $x_B$ and $n_U$ are independent and zero mean, while $\mathbb{E}\{|x_B|^2\} = P_B \sum_{i=1}^{K} \alpha_i = P_B$.

**Lemma 1** (*Exact and Relay-input-SNR Gains*). *The variable AF gain that satisfies the instantaneous UAV transmit-power constraint is*

$$G = \sqrt{\frac{\eta\rho P_B Z}{(1-\rho)(P_B Z + \sigma_U^2)}}. \tag{5}$$

*When $P_B Z \gg \sigma_U^2$, it reduces to*

$$G \approx \sqrt{\frac{\eta\rho}{1-\rho}}, \qquad G\sqrt{1-\rho} \approx \sqrt{\eta\rho}. \tag{6}$$

**Proof.** The relay transmits $x_U = G y_{\mathrm{IP}}$. Therefore, $\mathbb{E}\{|x_U|^2 \mid h_{BU}\} = G^2 P_{\mathrm{IP}}$. Enforcing $G^2 P_{\mathrm{IP}} = P_U$ and substituting the corresponding $P_U$ expression and (4) gives $G^2 = \frac{\eta\rho P_B Z}{(1-\rho)(P_B Z+\sigma_U^2)}$. Taking the nonnegative square root proves (5). Under $P_B Z \gg \sigma_U^2$, $P_B Z + \sigma_U^2 \approx P_B Z$, and hence $G \approx \sqrt{\frac{\eta\rho P_B Z}{(1-\rho)P_B Z}} = \sqrt{\frac{\eta\rho}{1-\rho}}$. Multiplication by $\sqrt{1-\rho}$ yields the second relation in (6). □

**Remark 1.** Section 3 first treats the exact variable gain and then develops a separate relay-input-SNR approximation based on (6). The approximation is invoked when $P_B Z/\sigma_U^2$ is large for a given realization; because outage emphasizes small $Z$, it need not become coefficient-exact merely by increasing the average transmit SNR.

### 2.3. Fluid antenna reception and spatial dependence

The $k$th user employs a FAS containing $N$ candidate ports. Let $h_{k,n}$ be the UAV–user-$k$ channel observed at port $n$. Its marginal distribution is $h_{k,n} \sim \mathcal{CN}(0, \Omega_k)$, and $\Omega_k = \beta_0 d_{Uk}^{-\nu_{Uk}}$, where $\nu_{Uk}$ is the second-hop path-loss exponent. Define $Y_{k,n} \triangleq |h_{k,n}|^2$. Each $Y_{k,n}$ has exponential marginal cumulative distribution function (CDF) and probability density function (PDF), respectively as $F_Y(y) = 1 - \exp\left(-\frac{y}{\Omega_k}\right)$, and $f_Y(y) = \frac{1}{\Omega_k}\exp\left(-\frac{y}{\Omega_k}\right)$. The active port is selected according to

$$n_k^\star = \arg\max_{1\le n\le N} Y_{k,n}, \tag{7}$$

which produces the effective gain

$$X_k \triangleq |h_{k,n_k^\star}|^2 = \max_{1\le n\le N} Y_{k,n}. \tag{8}$$

Because the candidate ports occupy a compact aperture, their gains may be statistically dependent. Let $\boldsymbol{R}_k = [r_{ij}^{(k)}]$ denote the physical complex-channel correlation matrix. For a linear aperture in isotropic scattering, a representative entry is

$$r_{ij}^{(k)} = J_0\left(\frac{2\pi d_{ij}}{\lambda}\right). \tag{9}$$

For jointly circular Gaussian channel samples, the associated Pearson correlation between the normalized power gains is

$$p_{ij}^{(k)} = \mathrm{corr}(Y_{k,i}, Y_{k,j}) = |r_{ij}^{(k)}|^2. \tag{10}$$

The latent Gaussian-copula matrix $\boldsymbol{C}_k = [c_{ij}^{(k)}]$ is not set equal to $\boldsymbol{R}_k$. Instead, for two standard Gaussian variables $(V_1, V_2)$ with correlation $c$, define

$$g(c) = \mathrm{corr}\left[-\ln(1-\Phi(V_1)), -\ln(1-\Phi(V_2))\right]. \tag{11}$$

Each off-diagonal entry is first obtained from $c_{ij}^{(k)} = g^{-1}(p_{ij}^{(k)})$. Because pairwise inversion does not always produce a positive-semidefinite matrix, the assembled matrix is projected onto the nearest correlation matrix. The resulting $\boldsymbol{C}_k$ is therefore a moment-matched surrogate whose accuracy for the selected gain is assessed numerically.

**Lemma 2** (*CDF of the Selected Gain Under a Gaussian Copula*). *Let the joint distribution of $(Y_{k,1}, \dots, Y_{k,N})$ be represented by a Gaussian copula with dependence matrix $\boldsymbol{C}_k$ and exponential marginals. Then*

$$F_{X_k}^{\mathrm{corr}}(x) = \boldsymbol{\Phi}_N\left(q_k(x)1_N; \boldsymbol{C}_k\right), \tag{12}$$

*where $q_k(x) \triangleq \Phi^{-1}\left(1-\exp\left(-\frac{x}{\Omega_k}\right)\right)$, $\Phi(\cdot)$ is the univariate standard Gaussian CDF, $\boldsymbol{\Phi}_N(\cdot;\boldsymbol{C}_k)$ is the $N$-variate standard Gaussian CDF, and $1_N$ is the all-one vector.*

**Proof.** By definition of the maximum,

$$F_{X_k}^{\mathrm{corr}}(x) = \Pr(X_k \le x)$$
$$= \Pr(Y_{k,1} \le x, \dots, Y_{k,N} \le x). \tag{13}$$

The Gaussian-copula representation of the joint CDF is

$$\Pr(Y_{k,1} \le y_1, \dots, Y_{k,N} \le y_N)$$
$$= \boldsymbol{\Phi}_N\left(\Phi^{-1}(F_Y(y_1)), \dots, \Phi^{-1}(F_Y(y_N)); \boldsymbol{C}_k\right). \tag{14}$$

Setting $y_1 = \cdots = y_N = x$, and defining $q_k(x)$ gives (12). □

**Lemma 3** (*PDF of the Correlated Selected Gain*). *For $x > 0$, the PDF corresponding to (12) can be written as*

$$f_{X_k}^{\mathrm{corr}}(x) = q_k'(x) \sum_{j=1}^{N} \frac{\partial \boldsymbol{\Phi}_N(\boldsymbol{v}; \boldsymbol{C}_k)}{\partial v_j}\bigg|_{\boldsymbol{v}=q_k(x)1_N}, \tag{15}$$

*where $q_k'(x) = \frac{f_Y(x)}{\phi(q_k(x))} = \frac{\Omega_k^{-1}\exp(-x/\Omega_k)}{\phi(q_k(x))}$, and $\phi(\cdot)$ denotes the standard Gaussian PDF. Equivalently,*

$$f_{X_k}^{\mathrm{corr}}(x) = f_Y(x) \sum_{j=1}^{N} \boldsymbol{\Phi}_{N-1}\left(q_k(x)1_{N-1}; \boldsymbol{\mu}_{-j|j}, \boldsymbol{\Sigma}_{-j|j}\right), \tag{16}$$

*with $\boldsymbol{\mu}_{-j|j} = \boldsymbol{c}_{-j,j}\, q_k(x)$, and $\boldsymbol{\Sigma}_{-j|j} = \boldsymbol{C}_{-j,-j} - \boldsymbol{c}_{-j,j}\boldsymbol{c}_{j,-j}$.*

**Proof.** Differentiate (12) with respect to $x$. Since every argument of the multivariate Gaussian CDF equals $q_k(x)$, the multivariate chain rule gives

$$\frac{d}{dx}\boldsymbol{\Phi}_N(q_k(x)1_N; \boldsymbol{C}_k) = q_k'(x) \sum_{j=1}^{N} \frac{\partial \boldsymbol{\Phi}_N(\boldsymbol{v}; \boldsymbol{C}_k)}{\partial v_j}\bigg|_{\boldsymbol{v}=q_k(x)1_N},$$

which proves (15). Next, $q_k(x) = \Phi^{-1}(F_Y(x))$. Differentiating the identity $\Phi(q_k(x)) = F_Y(x)$ yields $\phi(q_k(x))q_k'(x) = f_Y(x)$, and therefore $q_k'(x)$ follows. For a zero-mean multivariate Gaussian vector, differentiation of its CDF with respect to the $j$th upper limit gives the marginal density of the $j$th component multiplied by the conditional CDF of the remaining $N-1$ components. Thus,

$$\frac{\partial \boldsymbol{\Phi}_N(\boldsymbol{v}; \boldsymbol{C}_k)}{\partial v_j} = \phi(v_j)\,\boldsymbol{\Phi}_{N-1}\Big(\boldsymbol{v}_{-j}; \boldsymbol{c}_{-j,j}v_j, \boldsymbol{C}_{-j,-j} - \boldsymbol{c}_{-j,j}\boldsymbol{c}_{j,-j}\Big). \tag{17}$$

Substituting $v_j = q_k(x)$, multiplying by $q_k'(x) = f_Y(x)/\phi(q_k(x))$, and summing over $j$ proves (16). □

**Corollary 1** (*Independent-port Distribution*). *If the FAS ports are independent, then*

$$F_{X_k}^{\mathrm{ind}}(x) = \left[1-\exp\left(-\frac{x}{\Omega_k}\right)\right]^N, \tag{18}$$

$$f_{X_k}^{\mathrm{ind}}(x) = \frac{N}{\Omega_k}\exp\left(-\frac{x}{\Omega_k}\right)\left[1-\exp\left(-\frac{x}{\Omega_k}\right)\right]^{N-1}. \tag{19}$$

**Proof.** Independence gives

$$F_{X_k}^{\mathrm{ind}}(x) = \Pr(Y_{k,1} \le x, \dots, Y_{k,N} \le x)$$

$$= \prod_{n=1}^{N} \Pr(Y_{k,n} \le x)$$
$$= \prod_{n=1}^{N} F_Y(x)$$
$$= [F_Y(x)]^N,$$

which yields (18). Differentiating,

$$f_{X_k}^{\text{ind}}(x) = N[F_Y(x)]^{N-1} f_Y(x)$$
$$= \frac{N}{\Omega_k} \exp\left(-\frac{x}{\Omega_k}\right) \left[1 - \exp\left(-\frac{x}{\Omega_k}\right)\right]^{N-1},$$

which proves (19). □

### 2.4. Second transmission phase and end-to-end signal-to-interference-plus-noise ratio (SINR)

The signal received by $k$th user through its selected FAS port is

$$y_k = h_k^\star x_U + n_k, \tag{20}$$

where $h_k^\star = h_{k,n_k^\star}$ and $n_k \sim \mathcal{CN}(0, \sigma_k^2)$. Substituting $x_U = G y_{\text{IP}}$ and (3) gives

$$y_k = G\sqrt{1-\rho}\, h_k^\star h_{BU} \sum_{i=1}^{K} \sqrt{\alpha_i P_B}\, s_i + G\sqrt{1-\rho}\, h_k^\star n_U + n_k. \tag{21}$$

Let $a \triangleq \eta\rho$, assume $\sigma_U^2 = \sigma_k^2 = \sigma^2$, define $\bar{\gamma} = P_B/\sigma^2$, and set $t = \bar{\gamma} Z$. Substitution of the exact gain in (21) gives the exact layer SINR

$$\gamma_{k\to m}^{\text{ex}} = \frac{a\alpha_m t^2 X_k}{a A_m t^2 X_k + a t X_k + t + 1}, \qquad m \le k, \tag{22}$$

where $A_m = \sum_{i=m+1}^{K} \alpha_i$. Under the relay-input-SNR approximation in (6), the received signal becomes

$$y_k \approx \sqrt{a}\, h_k^\star h_{BU} \sum_{i=1}^{K} \sqrt{\alpha_i P_B}\, s_i + \sqrt{a}\, h_k^\star n_U + n_k, \tag{23}$$

and the corresponding approximate SINR is

$$\gamma_{k\to m}^{\text{ap}} = \frac{a\bar{\gamma}\alpha_m Z X_k}{a\bar{\gamma} Z X_k A_m + a X_k + 1}, \qquad m \le k. \tag{24}$$

### 2.5. Models used for practical robustness assessment

The preceding Rayleigh/linear-EH model is the basis of the exact closed-form analysis. To assess the principal practical departures without applying the Rayleigh expressions outside their assumptions, the numerical robustness study uses the following models. First, a Rician power gain $G_R$ with Rician factor $K_R$ and average power $\Omega$ has CDF

$$F_{G_R}(g) = 1 - Q_1\left(\sqrt{2K_R}, \sqrt{\frac{2(1+K_R)g}{\Omega}}\right), \tag{25}$$

where $Q_1(\cdot,\cdot)$ is the first-order Marcum-$Q$ function. For $N$ independent Rician FAS ports, $F_{X_k}(x) = [F_{G_R}(x)]^N$. Lemma 4 remains unchanged because it is conditional on the realized gains; only the CDFs used in the final averaging are replaced by (25).

Second, the linear harvested-power law is compared with the sensitivity-truncated logistic model [19]

$$P_U^{\text{nl}} = \begin{cases} 0, & P_{\text{in}} < P_{\text{sen}}, \\ \dfrac{M}{1-\Omega_0}\left(\dfrac{1}{1+e^{-a_h(P_{\text{in}}-b_h)}} - \Omega_0\right), & P_{\text{in}} \ge P_{\text{sen}}, \end{cases} \tag{26}$$

where $P_{\text{in}} = \rho P_B Z$, $\Omega_0 = (1+e^{a_h b_h})^{-1}$, $P_{\text{sen}}$ is the activation sensitivity, and $M$ is the saturation output. The corresponding variable gain is

$$G_{\text{nl}} = \sqrt{\frac{P_U^{\text{nl}}}{(1-\rho)(P_B Z + \sigma_U^2)}}. \tag{27}$$

Thus, nonlinear harvesting is evaluated through the input–output relation rather than by inserting a constant efficiency into the linear formulas.

Third, port-selection aging is represented by

$$\widetilde{h}_{k,n} = r_c h_{k,n} + \sqrt{1-r_c^2}\, e_{k,n}, \quad e_{k,n} \sim \mathcal{CN}(0, \Omega_k), \tag{28}$$

and the selected index maximizes $|\widetilde{h}_{k,n}|^2$ while outage is evaluated using the actual $|h_{k,n}|^2$. Residual SIC with leakage factor $\epsilon$ replaces $A_m$ in (22) by

$$A_m^{(\epsilon)} = \sum_{i=m+1}^{K} \alpha_i + \epsilon \sum_{i=1}^{m-1} \alpha_i. \tag{29}$$

The relay transmit-power constraint continues to use the actually harvested energy; (28) isolates the port-probing/selection error.

Finally, the predetermined service order is compared with instantaneous weak-to-strong ordering of the selected gains. Under the adaptive benchmark, power levels are reassigned after ranking $X_1, \dots, X_K$, and every physical user decodes the higher-power layers preceding its assigned layer. Equal target rates are used in this controlled comparison so that reordering does not also change the service requirements.

The single-antenna BS/UAV baseline isolates the energy-coupled AF and FAS effects. The conditioning structure accommodates a multi-antenna first hop by replacing $F_Z$ in Theorem 1 with the effective transmit-beamforming or receive-combining gain CDF. A multi-antenna UAV downlink additionally replaces $X_k$ by its post-beamforming selected-port gain and requires joint beamforming, power-allocation, and placement design; it is not represented by the scalar closed form.

## 3. Performance analysis

### 3.1. Exact decoding threshold and outage integral

Let $R_m$ denote the target end-to-end spectral efficiency of layer $m$. Since two equal phases are used, $\tau_m = 2^{2R_m} - 1$. Define $A_m = \sum_{i=m+1}^{K} \alpha_i$ and $\Delta_m = \alpha_m - \tau_m A_m$.

**Lemma 4** (*Exact Layer Threshold*). *For a selected gain $X_k = x > 0$, the exact condition $\gamma_{k\to m}^{\text{ex}} \ge \tau_m$ is feasible only if $\Delta_m > 0$. Under this condition it is equivalent to*

$$\bar{\gamma} Z \ge b_m(x), \tag{30}$$

*where*

$$b_m(x) = \frac{\tau_m(ax+1) + \sqrt{\tau_m^2(ax+1)^2 + 4ax\Delta_m\tau_m}}{2ax\Delta_m}. \tag{31}$$

**Proof.** Substitution of (22) and cross-multiplication give

$$ax\Delta_m t^2 - \tau_m(ax+1)t - \tau_m \ge 0, \qquad t = \bar{\gamma} Z.$$

If $\Delta_m \le 0$, every term on the left-hand side is nonpositive for $t \ge 0$, while the constant term is strictly negative; hence the inequality cannot hold. For $\Delta_m > 0$, the upward-opening quadratic is nonnegative for $t$ above its unique positive root, which is (31). □

Define

$$B_k(x) = \max_{1\le m\le k} b_m(x). \tag{32}$$

**Theorem 1** (*Exact One-dimensional Outage Integral*). *If $\Delta_m > 0$ for every $m \le k$, the exact outage probability for any selected-gain PDF $f_{X_k}(x)$ is*[2]

$$P_{\text{out},k}^{\text{ex}} = \int_0^\infty F_Z\left(\frac{B_k(x)}{\bar{\gamma}}\right) f_{X_k}(x)\, dx \tag{33}$$

[2] The single-antenna BS and UAV assumptions have been adopted for analytical tractability and simplicity. For a multi-antenna BS employing transmit beamforming, or a multi-antenna UAV employing receive combining during

$$= 1 - \int_0^\infty \exp\left[-\frac{B_k(x)}{\bar{\gamma}\Omega_{BU}}\right] f_{X_k}(x)\,dx. \tag{34}$$

*If any required $\Delta_m \le 0$, then $P_{\text{out},k}^{\text{ex}} = 1$.*

**Proof.** Successful recovery at user $k$ requires all layers $m = 1, \dots, k$ to satisfy (30), which is equivalent to $\bar{\gamma} Z \ge B_k(X_k)$. Conditioning on $X_k = x$ and using the exponential first-hop CDF gives (33) and (34). □

Eq. (34) applies to independent ports through (19) and to the calibrated correlated-port surrogate through (16). Unlike the approximate model below, $B_k(x)$ generally cannot be represented by the single scalar $\Theta_k$ because the exact roots depend separately on $\tau_m$ and $\Delta_m$.

### 3.2. Approximate decoding event

**Lemma 5** (*Approximate Layer Condition*). *For $m \le k$, $\gamma_{k\to m}^{\text{ap}} \ge \tau_m$ is feasible only when $\Delta_m > 0$ and is then equivalent to*

$$Z \ge \frac{\tau_m(aX_k + 1)}{a\bar{\gamma} X_k \Delta_m}. \tag{35}$$

**Proof.** Cross-multiplying (24) gives $a\bar{\gamma} Z X_k \Delta_m \ge \tau_m(aX_k + 1)$. The right-hand side is positive, which proves infeasibility for $\Delta_m \le 0$ and yields (35) otherwise. □

**Corollary 2** (*NOMA Feasibility*). *User $k$ is in certain outage under either relay model if*

$$\alpha_m \le \tau_m \sum_{i=m+1}^{K} \alpha_i \tag{36}$$

*for at least one $m \le k$.*

**Theorem 2** (*Unified Approximate Outage Event*). *Let $\theta_m = \tau_m/\Delta_m$ and $\Theta_k = \max_{1\le m\le k} \theta_m$. Then*

$$P_{\text{out},k}^{\text{ap}} = \Pr\left[Z < \frac{\Theta_k}{\bar{\gamma}} + \frac{\Theta_k}{a\bar{\gamma} X_k}\right]. \tag{37}$$

**Proof.** All approximate layer conditions hold if and only if $Z \ge [(aX_k + 1)/(a\bar{\gamma} X_k)] \max_{m\le k} \theta_m$. Taking the complement and separating the two terms gives (37). □

### 3.3. Correlated FAS

**Theorem 3** (*Approximate Outage Probability with Correlated FAS Ports*). *Under the Gaussian-copula FAS model of Lemma 2, the outage probability of $k$th user admits the following two equivalent one-dimensional representations:*

$$P_{\text{out},k}^{\text{ap,corr}} = 1 - \exp\left(-\frac{\Theta_k}{\bar{\gamma}\Omega_{BU}}\right) \times \int_0^\infty \exp\left(-\frac{\Theta_k}{a\bar{\gamma}\Omega_{BU} x}\right) f_{X_k}^{\text{corr}}(x)\,dx. \tag{38}$$

*and*

$$P_{\text{out},k}^{\text{ap,corr}} = F_Z\left(\frac{\Theta_k}{\bar{\gamma}}\right) + \int_{\Theta_k/\bar{\gamma}}^\infty F_{X_k}^{\text{corr}}\left(\frac{\Theta_k}{a(\bar{\gamma} z - \Theta_k)}\right) f_Z(z)\,dz. \tag{39}$$

*The second form requires only the copula CDF and is therefore convenient for numerical evaluation.*

**Proof.** Condition on $X_k = x$. From (37),

$$P_{\text{out},k}^{\text{ap,corr}} = \int_0^\infty F_Z\left(\frac{\Theta_k}{\bar{\gamma}} + \frac{\Theta_k}{a\bar{\gamma} x}\right) f_{X_k}^{\text{corr}}(x)\,dx. \tag{40}$$

Using the CDF of $Z$ and the normalization of $f_{X_k}^{\text{corr}}(x)$ gives

$$P_{\text{out},k}^{\text{ap,corr}} = 1 - \exp\left(-\frac{\Theta_k}{\bar{\gamma}\Omega_{BU}}\right) \times \int_0^\infty \exp\left(-\frac{\Theta_k}{a\bar{\gamma}\Omega_{BU} x}\right) f_{X_k}^{\text{corr}}(x)\,dx, \tag{41}$$

Since the PDF integrates to one, (38) follows.

For the second representation, condition instead on $Z = z$. From (37), outage occurs automatically when $z \le \frac{\Theta_k}{\bar{\gamma}}$, because the second term on the right-hand side is nonnegative. For $z > \Theta_k/\bar{\gamma}$, the outage inequality is $z < \frac{\Theta_k}{\bar{\gamma}} + \frac{\Theta_k}{a\bar{\gamma} X_k}$. Subtracting $\Theta_k/\bar{\gamma}$, $z - \frac{\Theta_k}{\bar{\gamma}} < \frac{\Theta_k}{a\bar{\gamma} X_k}$. Both sides are positive; therefore inversion reverses the inequality: $X_k < \frac{\Theta_k}{a\bar{\gamma}(z - \Theta_k/\bar{\gamma})} = \frac{\Theta_k}{a(\bar{\gamma} z - \Theta_k)}$. Applying the law of total probability gives

$$P_{\text{out},k}^{\text{ap,corr}} = \Pr\left(Z \le \frac{\Theta_k}{\bar{\gamma}}\right) + \int_{\Theta_k/\bar{\gamma}}^\infty \Pr\left(X_k < \frac{\Theta_k}{a(\bar{\gamma} z - \Theta_k)}\right) f_Z(z)\,dz,$$

which is precisely (39). □

**Corollary 3** (*Independent-port Limit of the Copula Expression*). *When $\boldsymbol{C}_k = \boldsymbol{I}_N$,*

$$\boldsymbol{\Phi}_N(q\mathbf{1}_N; \boldsymbol{I}_N) = [\Phi(q)]^N.$$

*Since $\Phi(q_k(x)) = F_Y(x)$,*

$$F_{X_k}^{\text{corr}}(x) = [F_Y(x)]^N = F_{X_k}^{\text{ind}}(x).$$

*Hence, Theorem 3 continuously reduces to the independent-FAS result.*

### 3.4. Independent FAS: closed-form outage probability

**Theorem 4** (*Closed-form Approximate Outage Probability for Independent Ports*). *For $N$ independent and identically distributed FAS ports, the outage probability of the $k$th user is*

$$P_{\text{out},k}^{\text{ap,ind}} = 1 - 2\exp\left(-\frac{\Theta_k}{\bar{\gamma}\Omega_{BU}}\right) \sum_{n=1}^{N} (-1)^{n+1} \binom{N}{n} \times \sqrt{\frac{n\Theta_k}{a\bar{\gamma}\Omega_{BU}\Omega_k}} K_1\left(2\sqrt{\frac{n\Theta_k}{a\bar{\gamma}\Omega_{BU}\Omega_k}}\right), \tag{42}$$

*where $K_1(\cdot)$ is the modified Bessel function of the second kind and order one.*

**Proof.** Conditioning on $X_k = x$ and using (37),

$$P_{\text{out},k}^{\text{ap,ind}} = \int_0^\infty F_Z\left(\frac{\Theta_k}{\bar{\gamma}} + \frac{\Theta_k}{a\bar{\gamma} x}\right) f_{X_k}^{\text{ind}}(x)\,dx. \tag{43}$$

Substitution of $F_Z$ gives

$$P_{\text{out},k}^{\text{ap,ind}} = 1 - \exp\left(-\frac{\Theta_k}{\bar{\gamma}\Omega_{BU}}\right) \mathcal{I}_k, \tag{44}$$

where

$$\mathcal{I}_k \triangleq \int_0^\infty \exp\left(-\frac{\Theta_k}{a\bar{\gamma}\Omega_{BU} x}\right) f_{X_k}^{\text{ind}}(x)\,dx. \tag{45}$$

Substituting (19),

$$\mathcal{I}_k = \frac{N}{\Omega_k} \int_0^\infty \exp\left(-\frac{x}{\Omega_k} - \frac{\Theta_k}{a\bar{\gamma}\Omega_{BU} x}\right) \times \left[1 - \exp\left(-\frac{x}{\Omega_k}\right)\right]^{N-1} dx. \tag{46}$$

---

the first transmission phase, *Theorem 1* remains applicable after replacing $F_Z(\cdot)$ with the CDF of the corresponding effective first-hop channel gain. A multi-antenna UAV downlink additionally requires replacing $X_k$ with the post-beamforming selected-port gain and may require the joint design of beamforming, NOMA power allocation, and UAV placement; therefore, additional derivations would be required for the resulting closed-form expressions.

Apply the binomial expansion

$$(1-u)^{N-1} = \sum_{\ell=0}^{N-1} (-1)^{\ell} \binom{N-1}{\ell} u^{\ell} \tag{47}$$

with $u = \exp(-x/\Omega_k)$:

$$\left[1 - \exp\left(-\frac{x}{\Omega_k}\right)\right]^{N-1} = \sum_{\ell=0}^{N-1} (-1)^{\ell} \binom{N-1}{\ell} \exp\left(-\frac{\ell x}{\Omega_k}\right). \tag{48}$$

Consequently,

$$\mathcal{I}_k = \frac{N}{\Omega_k} \sum_{\ell=0}^{N-1} (-1)^{\ell} \binom{N-1}{\ell} \times \int_0^{\infty} \exp\left[-\frac{(\ell+1)x}{\Omega_k} - \frac{\Theta_k}{a\bar{\gamma}\Omega_{BU}x}\right] dx. \tag{49}$$

The standard integral

$$\int_0^{\infty} \exp\left(-\beta x - \frac{\delta}{x}\right) dx = 2\sqrt{\frac{\delta}{\beta}} K_1(2\sqrt{\beta\delta}), \tag{50}$$

is now used with

$$\beta_{\ell} = \frac{\ell+1}{\Omega_k}, \qquad \delta_k = \frac{\Theta_k}{a\bar{\gamma}\Omega_{BU}}. \tag{51}$$

Thus,

$$\int_0^{\infty} \exp\left[-\frac{(\ell+1)x}{\Omega_k} - \frac{\Theta_k}{a\bar{\gamma}\Omega_{BU}x}\right] dx = 2\sqrt{\frac{\Theta_k\Omega_k}{(\ell+1)a\bar{\gamma}\Omega_{BU}}} K_1\left(2\sqrt{\frac{(\ell+1)\Theta_k}{a\bar{\gamma}\Omega_{BU}\Omega_k}}\right). \tag{52}$$

Substitution into (49) gives

$$\mathcal{I}_k = 2N \sum_{\ell=0}^{N-1} (-1)^{\ell} \binom{N-1}{\ell} \times \sqrt{\frac{\Theta_k}{(\ell+1)a\bar{\gamma}\Omega_{BU}\Omega_k}} K_1\left(2\sqrt{\frac{(\ell+1)\Theta_k}{a\bar{\gamma}\Omega_{BU}\Omega_k}}\right). \tag{53}$$

Combining (44) and (53) already yields a closed form. To obtain the more compact representation in (42), set $n = \ell + 1$. Then $N\binom{N-1}{n-1} = n\binom{N}{n}$, and $n\sqrt{\frac{\Theta_k}{n}} = \sqrt{n\Theta_k}$. Moreover, $(-1)^{n-1} = (-1)^{n+1}$. Applying these identities to (53) and substituting the result into (44) completes the proof. □

**Corollary 4** (*Single-port Receiver*). *For $N = 1$, (42) reduces to*

$$P_{\text{out},k}^{\text{ap},(N=1)} = 1 - 2\exp\left(-\frac{\Theta_k}{\bar{\gamma}\Omega_{BU}}\right)\sqrt{\frac{\Theta_k}{a\bar{\gamma}\Omega_{BU}\Omega_k}} \times K_1\left(2\sqrt{\frac{\Theta_k}{a\bar{\gamma}\Omega_{BU}\Omega_k}}\right). \tag{54}$$

### 3.5. High-SNR behavior

**Theorem 5** (*Finite-inverse-moment Asymptotics*). *Suppose $\mathbb{E}[B_k(X_k)] < \infty$. Then the exact model satisfies*

$$P_{\text{out},k}^{\text{ex}} = \frac{\mathbb{E}[B_k(X_k)]}{\bar{\gamma}\Omega_{BU}} + o(\bar{\gamma}^{-1}). \tag{55}$$

*If $\mathbb{E}[X_k^{-1}] < \infty$, the approximate model satisfies*

$$P_{\text{out},k}^{\text{ap}} = \frac{\Theta_k}{\bar{\gamma}\Omega_{BU}}\left(1 + \frac{\mathbb{E}[X_k^{-1}]}{a}\right) + o(\bar{\gamma}^{-1}). \tag{56}$$

*Consequently, both models have diversity order one under these conditions.*

**Proof.** For the exact model, multiply (33) by $\bar{\gamma}$ and use $\bar{\gamma}[1-\exp(-u/\bar{\gamma})] \to u$ together with dominated convergence. For the approximate model, apply the same argument to the random threshold $\Theta_k[1+(aX_k)^{-1}]$. The diversity result follows from $-\lim_{\bar{\gamma}\to\infty} \log P_{\text{out}} / \log \bar{\gamma} = 1$. □

For independent exponential ports with $N > 1$,

$$\mathbb{E}[X_k^{-1}] = -\frac{N}{\Omega_k} \sum_{\ell=0}^{N-1} (-1)^{\ell} \binom{N-1}{\ell} \ln(\ell+1), \tag{57}$$

which is finite. For a correlated selected gain, Theorem 5 is stated conditionally because the lower-tail dependence determines whether the inverse moment exists. A nondegenerate calibrated Gaussian copula normally yields a finite inverse moment for multiple ports, whereas the perfectly correlated limit reduces to the single-port case.

**Corollary 5** (*Independent Single-port Asymptotics*). *For $N = 1$,*

$$P_{\text{out},k}^{\text{ap}} = \frac{\Theta_k}{a\Omega_{BU}\Omega_k}\frac{\ln\bar{\gamma}}{\bar{\gamma}} + \mathcal{O}(\bar{\gamma}^{-1}). \tag{58}$$

*The exact model has the same leading logarithmic term. Thus, the diversity order is one, but a finite conventional coding-gain coefficient multiplying only $1/\bar{\gamma}$ does not exist.*

**Proof.** Expanding $K_1(z)$ in (54) for small $z$ gives (58). For the exact model, (31) implies $B_k(x) \sim \Theta_k/(ax)$ as $x \downarrow 0$, which produces the same logarithmic leading term after integration over the exponential single-port density. □

**Remark 2.** The exact and approximate asymptotic coefficients in (55) and (56) are generally different. Hence the relay-input-SNR approximation can preserve diversity order while retaining a nonzero relative outage error at high average SNR.

### 3.6. Delay-limited throughput

Because $R_k$ is already defined as an end-to-end spectral efficiency and the factor $1/2$ has already been included through $2^{2R_k} - 1$, the delay-limited goodput of the $k$th user is

$$\mathcal{T}_k = R_k\left(1 - P_{\text{out},k}\right). \tag{59}$$

The sum throughput is therefore

$$\mathcal{T}_{\text{sum}} = \sum_{k=1}^{K} R_k\left(1 - P_{\text{out},k}\right). \tag{60}$$

For correlated and independent FAS ports, respectively,

$$\mathcal{T}_{\text{sum}}^{\text{corr}} = \sum_{k=1}^{K} R_k\left(1 - P_{\text{out},k}^{\text{ap,corr}}\right), \tag{61}$$

$$\mathcal{T}_{\text{sum}}^{\text{ind}} = \sum_{k=1}^{K} R_k\left(1 - P_{\text{out},k}^{\text{ap,ind}}\right). \tag{62}$$

**Remark 3** (*Alternative Rate Convention*). If $R_k^{\text{src}}$ is instead defined as the source coding rate before the half-duplex loss, then one should use

$$\tau_k = 2^{R_k^{\text{src}}} - 1$$

and

$$\mathcal{T}_k = \frac{1}{2}R_k^{\text{src}}(1 - P_{\text{out},k}).$$

The two conventions are equivalent when applied consistently; the half-duplex factor must not be inserted twice.

### 3.7. Energy efficiency

Let $E_{\text{ext}}$ denote the energy drawn from non-harvested sources during one complete block. The corresponding average external power is

$$\bar{P}_{\text{ext}} = \frac{E_{\text{ext}}}{T}. \tag{63}$$

A phase-aware model is

$$E_{\text{ext}} = \frac{T}{2}\left(\xi_B P_B + P_{c,B}^{(1)} + P_{c,U}^{\text{rx}}\right)$$

$$+\frac{T}{2}\left(P_{c,U}^{\mathrm{tx}}+\sum_{k=1}^{K}P_{c,k}\right), \tag{64}$$

where the UAV RF forwarding power is not added because it is supplied by the harvested energy. Accordingly,

$$\bar{P}_{\mathrm{ext}}=\frac{1}{2}\left(\xi_B P_B+P_{c,B}^{(1)}+P_{c,U}^{\mathrm{rx}}+P_{c,U}^{\mathrm{tx}}+\sum_{k=1}^{K}P_{c,k}\right). \tag{65}$$

If the circuit powers are already defined as block-averaged quantities, a simplified model may be written as

$$\bar{P}_{\mathrm{ext}}=\frac{\xi_B P_B}{2}+P_{c,B}+P_{c,U}+\sum_{k=1}^{K}P_{c,k}. \tag{66}$$

The external-source communication energy efficiency, measured in bit/J/Hz, is

$$\mathrm{EE}=\frac{\mathcal{T}_{\mathrm{sum}}}{\bar{P}_{\mathrm{ext}}}. \tag{67}$$

Hence,

$$\mathrm{EE}^{\mathrm{corr}}=\frac{\sum_{k=1}^{K}R_k\left(1-P_{\mathrm{out},k}^{\mathrm{ap,corr}}\right)}{\bar{P}_{\mathrm{ext}}}, \tag{68}$$

$$\mathrm{EE}^{\mathrm{ind}}=\frac{\sum_{k=1}^{K}R_k\left(1-P_{\mathrm{out},k}^{\mathrm{ap,ind}}\right)}{\bar{P}_{\mathrm{ext}}}. \tag{69}$$

**Corollary 6** (*Reliability-throughput-energy-efficiency Relation*). *For fixed target rates and fixed external power consumption, $\mathcal{T}_{\mathrm{sum}}$ and* EE *are strictly decreasing functions of each user's outage probability. In particular,*

$$\frac{\partial\mathcal{T}_{\mathrm{sum}}}{\partial P_{\mathrm{out},k}}=-R_k<0, \tag{70}$$

$$\frac{\partial\mathrm{EE}}{\partial P_{\mathrm{out},k}}=-\frac{R_k}{\bar{P}_{\mathrm{ext}}}<0. \tag{71}$$

**Proof.** Differentiate (60) with respect to $P_{\mathrm{out},k}$:

$$\frac{\partial}{\partial P_{\mathrm{out},k}}\sum_{j=1}^{K}R_j(1-P_{\mathrm{out},j})=-R_k.$$

Since $R_k>0$, the derivative is negative. Dividing the sum throughput by the positive constant $\bar{P}_{\mathrm{ext}}$ and differentiating gives (71). □

### 3.8. Bounded weighted-centroid benchmark

Let the fixed-altitude feasible region be $\mathcal{Q}=[x_{\min},x_{\max}]\times[y_{\min},y_{\max}]$. For nonnegative geometric weights $\upsilon_B>0$ and $\upsilon_k\geq 0$, consider

$$\mathbf{P1}:\quad \min_{(x_{UAV},y_{UAV})\in\mathcal{Q}}\ \upsilon_B\|\boldsymbol{q}_{UAV}^{\mathrm{h}}-\boldsymbol{q}_{BS}^{\mathrm{h}}\|_2^2+\sum_{k=1}^{K}\upsilon_k\|\boldsymbol{q}_{UAV}^{\mathrm{h}}-\boldsymbol{q}_k^{\mathrm{h}}\|_2^2, \tag{72}$$

where the superscript h denotes horizontal coordinates. Define

$$\tilde{\boldsymbol{q}}_{UAV}^{\mathrm{h}}=\frac{\upsilon_B\boldsymbol{q}_{BS}^{\mathrm{h}}+\sum_{k=1}^{K}\upsilon_k\boldsymbol{q}_k^{\mathrm{h}}}{\upsilon_B+\sum_{k=1}^{K}\upsilon_k}. \tag{73}$$

**Theorem 6** (*Globally Optimal Bounded Weighted Centroid*). *Problem (72) is strictly convex and its unique solution is the coordinate-wise projection*

$$\boldsymbol{q}_{UAV,\mathrm{wc}}^{\star}=\Pi_{\mathcal{Q}}\left(\tilde{\boldsymbol{q}}_{UAV}^{\mathrm{h}}\right). \tag{74}$$

**Proof.** The Hessian is $2(\upsilon_B+\sum_k\upsilon_k)\boldsymbol{I}_2\succ 0$. Setting the gradient to zero gives (73); separability of the box constraints then gives the coordinate-wise projection. □

The unweighted centroid is recovered with $\upsilon_B=\upsilon_k=1$. The priority-weighted benchmark used numerically sets $\upsilon_B=1$ and $\upsilon_k=\omega_k$. This benchmark is geometric and is not claimed to optimize outage.

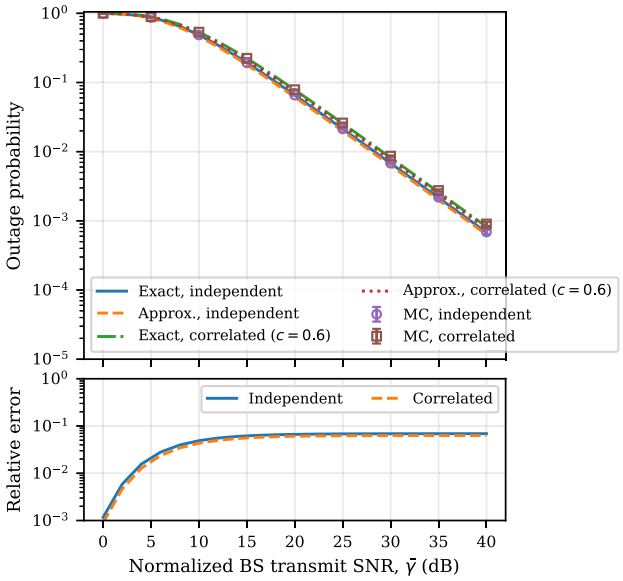



**Fig. 1.** Exact and approximate outage probabilities of user $k=2$ versus normalized BS transmit SNR. Markers and confidence intervals correspond to exact variable-gain Monte Carlo (MC) simulation.

### 3.9. Exact and approximate outage-aware placement

For $r\in\{\mathrm{ex},\mathrm{ap}\}$, define

$$\mathcal{J}^{r}(x_{UAV},y_{UAV})=\sum_{k=1}^{K}\omega_k P_{\mathrm{out},k}^{r}(x_{UAV},y_{UAV}),\qquad \sum_k\omega_k=1, \tag{75}$$

where the position dependence follows from $\Omega_{BU}=\beta_0 d_{BU}^{-\nu_{BU}}$ and $\Omega_k=\beta_0 d_{Uk}^{-\nu_{Uk}}$. The exact target problem is

$$\mathbf{P2}_{\mathrm{ex}}:\quad \min_{(x_{UAV},y_{UAV})\in\mathcal{Q}}\mathcal{J}^{\mathrm{ex}}(x_{UAV},y_{UAV}), \tag{76}$$

while $\mathbf{P2}_{\mathrm{ap}}$ replaces $\mathcal{J}^{\mathrm{ex}}$ by $\mathcal{J}^{\mathrm{ap}}$ to provide a lower-cost surrogate. Minimizing (75) is equivalent to maximizing $\sum_k\omega_k(1-P_{\mathrm{out},k})$. It is equivalent to weighted throughput only for equal target rates or when the objective weights are redefined to include $R_k$.

To reduce the global online search, approximate optima are generated offline for states

$$\boldsymbol{s}=[x_1,y_1,\ldots,x_K,y_K,\omega_1,\ldots,\omega_K,P_B,H,\rho]^T. \tag{77}$$

All other physical and NOMA parameters remain fixed during this experiment. After standardizing every feature using the training set, an inverse-distance $L$-nearest-neighbor predictor gives

$$\hat{\boldsymbol{q}}_{UAV,0}=\Pi_{\mathcal{Q}}\left(\frac{\sum_{i\in\mathcal{N}_L(s)}d_i^{-1}\boldsymbol{q}_{UAV,i}^{\mathrm{ap}}}{\sum_{i\in\mathcal{N}_L(s)}d_i^{-1}}\right), \tag{78}$$

where $d_i$ is the standardized Euclidean distance and $\boldsymbol{q}_{U,i}^{\mathrm{ap}}$ is an offline solution of $\mathbf{P2}_{\mathrm{ap}}$. The neighbor count $L$ is selected only on the validation set.

The predictor is used as an initialization rather than being presented as a one-pass optimizer. A $5\times 5$ local candidate grid centered on (78) is evaluated with $\mathcal{J}^{\mathrm{ap}}$, and the best candidate is polished by a bounded local search. This procedure uses 25 local grid points instead of the 399 points in the full $21\times 19$ initialization. For scientific validation, the resulting coordinates and all baselines are finally evaluated using $\mathcal{J}^{\mathrm{ex}}$, and an exact grid-plus-refinement solution is used as the test reference.

## 4. Numerical results and discussion

This section separates four roles of the models. Fig. 1 validates the exact integral and the relay-input-SNR approximation. Figs. 3–7 use

**Table 1**
Default numerical parameters.

| Parameter | Value |
|---|---|
| $K$, $\boldsymbol{\alpha}$, $(R_1, R_2, R_3)$ | 3, [0.60, 0.25, 0.15], (0.2, 0.3, 0.4) |
| $N$, $\rho$, $\eta$ | 8, 0.5, 0.8 |
| Normalized gains (baseline studies) | $\Omega_{BU} = \Omega_k = 1$ |
| $\beta_0$, $\nu_{BU}$, $\nu_{Uk}$ | −30 dB, 2.2, 2.6 |
| Noise powers | −90 dBm (EE), −160 dBm (placement) |
| BS PA factor, $\xi_B$ | 2.5 |
| Circuit powers | $P_{c,B}^{(1)} = 0.04$, $P_{c,U}^{\mathrm{rx}} = 0.03$ W<br>$P_{c,U}^{\mathrm{tx}} = 0.05$, $P_{c,k} = 0.01$ W |
| Copula/MC samples | $2^{18}/10^6$ (Fig. 1) |
| Rician factors | $K_R \in \{3, 6, 10\}$ dB |
| Nonlinear EH [19] | $M = 24$ mW, $a_h = 150$ W$^{-1}$, $b_h = 0.014$ W |
| Robustness errors | $r_c = 0.9$, $\epsilon = 0.02$ |

the approximate expressions for controlled parameter studies. Figs. 2 and 6 test the exact link against LoS fading and practical nonidealities. Finally, Figs. 8 and 9 optimize the approximate placement objective but evaluate every reported coordinate with the exact variable-gain objective.

Unless otherwise stated, $K = 3$, $\boldsymbol{\alpha} = [0.60, 0.25, 0.15]$, $(R_1, R_2, R_3) = (0.2, 0.3, 0.4)$ bit/s/Hz, $\eta = 0.8$, $\rho = 0.5$, and $N = 8$. These values follow the operating ranges used in UAV–SWIPT and UAV–NOMA studies [6,12,17,18]. The resulting thresholds are $\Theta_1 \approx 0.677$, $\Theta_2 \approx 2.987$, and $\Theta_3 \approx 4.941$. Normalized outage studies use $\Omega_{BU} = \Omega_k = 1$. The placement scenario uses the BS at $(0, 0)$ m, users at $(250, -150)$ m, $(450, 0)$ m, and $(300, 200)$ m, altitude $H = 100$ m, and region $[-50, 500] \times [-250, 250]$ m$^2$. The −90 dBm noise value is used only in the physical-power throughput/EE and nonlinear-EH studies. The placement experiment is a separately normalized ultra-narrowband case with effective post-processing noise −160 dBm; no absolute-power comparison is made between these two experiments, and every placement method uses the same noise value. This separation is now stated to remove the former ambiguity.

### 4.1. Exact-model and approximation validation

Fig. 1 compares the exact variable-gain outage integral, the approximate analytical expressions, and exact-model Monte Carlo estimates for user $k = 2$. The analytical exact curves agree with Monte Carlo simulation over the complete SNR range. At $\bar{\gamma} = 30$ dB, the exact outage probabilities are $6.79 \times 10^{-3}$ and $8.19 \times 10^{-3}$ for independent ports and correlated ports with $c = 0.6$, respectively. The corresponding approximate values are $6.32 \times 10^{-3}$ and $7.68 \times 10^{-3}$. At 40 dB, the exact values decrease to $6.81 \times 10^{-4}$ and $8.23 \times 10^{-4}$, whereas the approximation gives $6.34 \times 10^{-4}$ and $7.71 \times 10^{-4}$. The approximate model therefore preserves the high-SNR slope but underestimates the outage by approximately 6.87% and 6.29% in the independent and correlated cases at 40 dB. The relative error approaches a nonzero value because outage is governed by small first-hop realizations, for which the relay-input-SNR assumption is least accurate. This agrees with the different asymptotic coefficients in Theorem 5; only the diversity slope is shared.

To examine the approximation beyond the displayed setting, Table 2 varies the number of ports, the power-splitting ratio, and an AR(1) latent-copula correlation at 30 dB. Define the signed error as $100(P_{\mathrm{out}}^{\mathrm{ap}} - P_{\mathrm{out}}^{\mathrm{ex}})/P_{\mathrm{out}}^{\mathrm{ex}}$. The approximation remains optimistic in every case, with errors from −1.77% to −6.85%. Hence it is useful as an optimization surrogate, but exact reliability values should be retained for final assessment.

### 4.2. Sensitivity to LoS-dominant rician fading

The closed-form analysis uses Rayleigh fading, but UAV links often contain a dominant LoS component. Fig. 2 therefore evaluates the exact conditional formulation under unit-mean Rician fading on both hops. The same $K_R$ is used on the BS–UAV and UAV–user links, and independent FAS ports isolate the LoS effect from the spatial-dependence effect already studied separately. Eq. (25) and $F_{X_k}(x) = [F_{G_R}(x)]^N$ are substituted into Theorem 1; no Rayleigh closed form is reused. At 30 dB, user-2 outage decreases from $6.79 \times 10^{-3}$ under Rayleigh fading to $2.97 \times 10^{-3}$, $7.48 \times 10^{-4}$, and $6.03 \times 10^{-6}$ for $K_R = 3$, 6, and 10 dB, respectively. Thus, the LoS component suppresses the deep fades that govern the two-hop outage event. This result supports the qualitative FAS/SWIPT conclusions while restricting the Rayleigh closed forms to their stated baseline.

**Table 2**
Exact–approximate robustness for user $k = 2$ at 30 dB.

| $N$ | Dependence | $\rho$ | Exact | Approx. | Error (%) |
|---|---|---|---|---|---|
| 1 | Independent | 0.5 | 0.03916 | 0.03847 | −1.77 |
| 4 | Independent | 0.5 | 0.00856 | 0.00802 | −6.26 |
| 8 | Independent | 0.2 | 0.01196 | 0.01130 | −5.52 |
| 8 | Independent | 0.5 | 0.00679 | 0.00632 | −6.85 |
| 8 | Independent | 0.8 | 0.00544 | 0.00507 | −6.70 |
| 8 | AR(1), $c = 0.3$ | 0.5 | 0.00716 | 0.00668 | −6.71 |
| 8 | AR(1), $c = 0.6$ | 0.5 | 0.00820 | 0.00769 | −6.27 |
| 8 | AR(1), $c = 0.9$ | 0.5 | 0.01415 | 0.01355 | −4.22 |

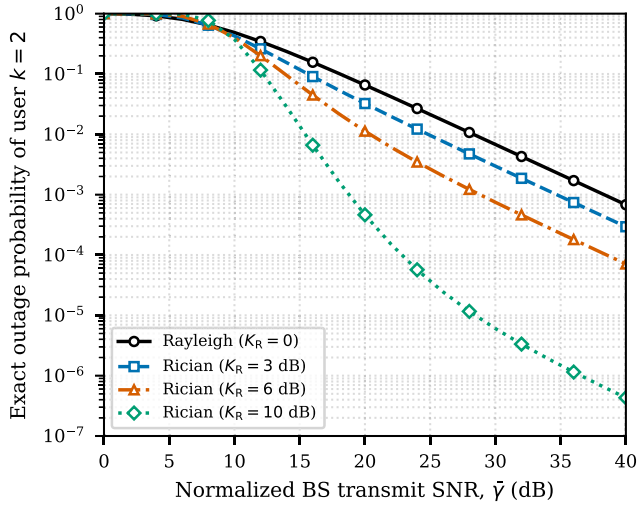



**Fig. 2.** Exact outage probability of user $k = 2$ under Rayleigh and unit-mean Rician fading. The same Rician factor is used on both hops; $N = 8$ independent FAS ports isolate the LoS effect.

### 4.3. Approximate outage versus port count and dependence

Fig. 3 uses the approximate outage probability for all curves. At 30 dB, the single-port result is $3.85 \times 10^{-2}$, whereas independent FAS configurations with $N = 4$ and $N = 8$ achieve $8.02 \times 10^{-3}$ and $6.32 \times 10^{-3}$, respectively. For $N = 8$, increasing the latent correlation from $c = 0.3$ to $c = 0.6$ and $c = 0.9$ increases the approximate outage from $6.68 \times 10^{-3}$ to $7.68 \times 10^{-3}$ and $1.35 \times 10^{-2}$. At 40 dB, the corresponding values are $6.70 \times 10^{-4}$, $7.71 \times 10^{-4}$, and $1.42 \times 10^{-3}$. The nearly parallel high-SNR curves confirm that additional and less-correlated ports improve the coding gain, whereas the common BS–UAV hop retains diversity order one. The $N = 1$ curve is the conventional fixed-antenna benchmark. Externally powered relaying is not treated as a like-for-like baseline because it changes the relay energy budget. A UAV–OMA–FAS reference is instead introduced separately in Fig. 10 under equal user-time allocation to provide a classical multiple-access benchmark without altering the SWIPT relay model.

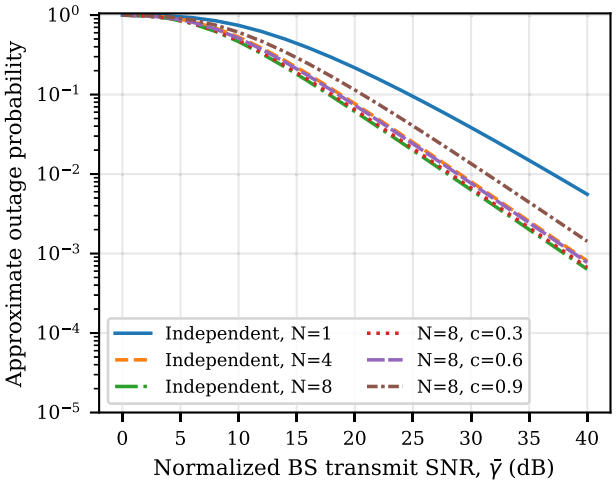



**Fig. 3.** Approximate outage probability of user $k = 2$ versus normalized BS transmit SNR for different numbers of FAS ports and latent Gaussian-copula dependence levels.

**Table 3**
Calibrated-copula validation against physical complex channels.

| $N$ | $W/\lambda$ | Max. corr. err. | KS | CDF RMSE |
|---|---|---|---|---|
| 4 | 0.6 | 0.0050 | 0.0196 | 0.0123 |
| 8 | 1.4 | 0.0219 | 0.0322 | 0.0232 |
| 16 | 1.4 | 0.0373 | 0.0535 | 0.0391 |

### 4.4. Approximate outage under fixed spacing and fixed aperture

Fig. 4 compares independent ports, a fixed normalized spacing of $d/\lambda = 0.2$, and a fixed aperture of $W/\lambda = 1.4$ at 30 dB. For independent ports, the approximate outage decreases from $1.30 \times 10^{-2}$ at $N = 2$ to $5.48 \times 10^{-3}$ at $N = 16$. With fixed spacing, it decreases from $1.81 \times 10^{-2}$ to $5.81 \times 10^{-3}$ because the physical aperture grows with $N$. Under a fixed aperture, the outage improves initially but saturates near $6.75 \times 10^{-3}$ as the ports become densely packed and increasingly dependent. The calibrated model does not interpret a negative Jakes coefficient as a negative power-gain correlation. Table 3 compares the surrogate with samples from the physical correlated complex Gaussian model. The selected-gain CDF error remains small for the tested apertures but increases as a fixed aperture is populated more densely and the nearest-correlation projection becomes active. The copula is therefore used as a validated tractable surrogate rather than an exact physical identity.

### 4.5. Approximate outage versus power splitting

Fig. 5 presents the approximate outage probabilities of all three users at 30 dB. For independent ports, increasing $\rho$ from 0.1 to 0.9 reduces the outage from $4.47 \times 10^{-3}$ to $1.10 \times 10^{-3}$ for user 1, from $1.95 \times 10^{-2}$ to $4.84 \times 10^{-3}$ for user 2, and from $3.21 \times 10^{-2}$ to $7.99 \times 10^{-3}$ for user 3. Correlation increases all outage probabilities but does not change the monotonic trend. Under the adopted ideal power-splitting model and relay-gain approximation, $\rho$ enters through $a = \eta\rho$, and no interior reliability-optimal value is produced. This behavior should not be generalized to nonlinear EH, saturation, or additional post-splitting conversion noise.

### 4.6. Nonlinear EH, imperfect CSI/SIC, and order adaptation

Fig. 6(a) compares the ideal linear harvester with (26). The nonlinear experiment uses $M = 24$ mW, $a_h = 150$ W$^{-1}$, $b_h = 0.014$ W, $P_{\text{sen}} = -20$ dBm, $\Omega_k = 10^{-4}$, and $-90$ dBm receiver noise. At an average

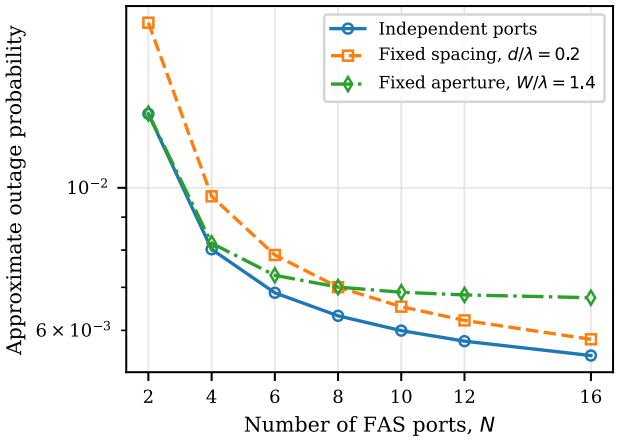



**Fig. 4.** Approximate outage probability versus the number of FAS ports under fixed spacing, fixed physical aperture with calibrated copula dependence, and independent-port reception.

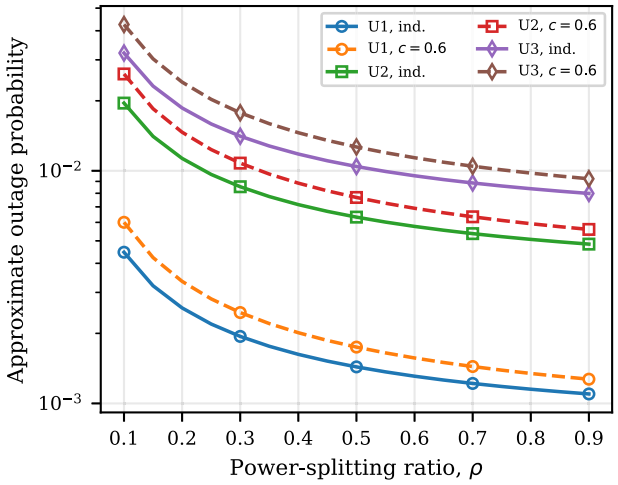



**Fig. 5.** Approximate outage probability of the three NOMA users versus the power-splitting ratio for independent and correlated FAS ports.

first-hop RF power of 0 dBm, user-2 outage is $9.0 \times 10^{-6}$ under the linear abstraction but $1.90 \times 10^{-2}$ under the nonlinear circuit. At 20 dBm, the nonlinear outage is still $1.64 \times 10^{-4}$ because activation and saturation limit the useful forwarding power. Hence, the linear model can substantially overestimate reliability and should be interpreted as an ideal benchmark.

Fig. 6(b) evaluates the actual selected-port gain after the aged estimate in (28) and uses (29) for imperfect cancellation. At 30 dB, the perfect-CSI/SIC outage is $6.72 \times 10^{-3}$; aged port CSI with $r_c = 0.9$ raises it to $8.35 \times 10^{-3}$, residual SIC with $\epsilon = 0.02$ raises it to $6.96 \times 10^{-3}$, and their joint effect gives $8.61 \times 10^{-3}$. The joint degradation is approximately 28%, confirming that the ideal analysis is a performance bound rather than an implementation prediction.

Fig. 6(c) compares predetermined and instantaneous weak-to-strong ordering in a controlled $K = 3$, $N = 4$ experiment with equal rates $R_k = 0.3$ bit/s/Hz and average selected-port scales proportional to $(0.8, 1, 1.2)$. At 30 dB, instantaneous reordering reduces mean user outage from $7.25 \times 10^{-3}$ to $6.83 \times 10^{-3}$. The gain is moderate because FAS selection concentrates each user's effective gain, but it confirms that the fixed service order is not dynamically optimal. The fixed order remains useful when service priority, signaling delay, and order-switching overhead preclude per-block reordering.

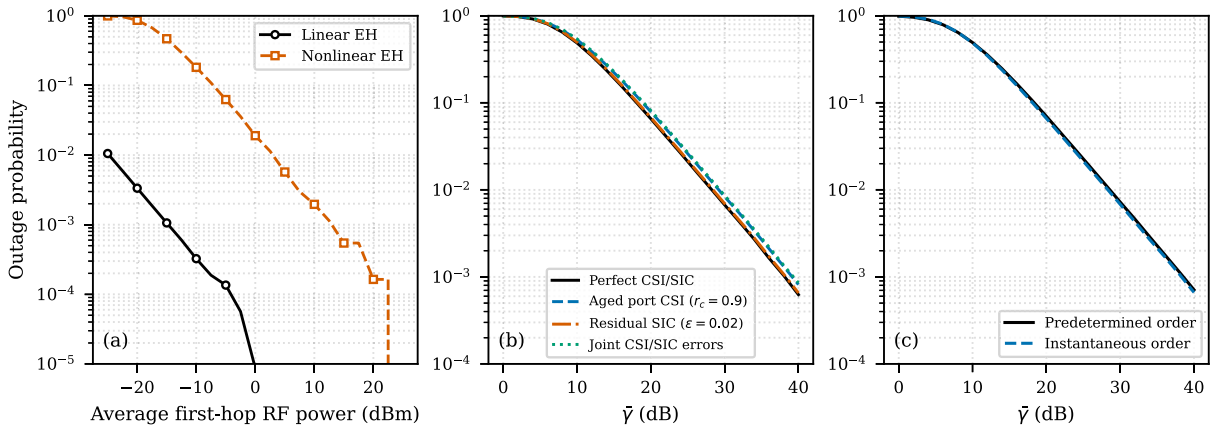



**Fig. 6.** Practical robustness of the exact variable-gain model: (a) ideal linear versus sensitivity-and-saturation nonlinear EH; (b) aged FAS port-selection CSI, residual SIC, and their joint effect; and (c) predetermined versus instantaneous NOMA ordering.

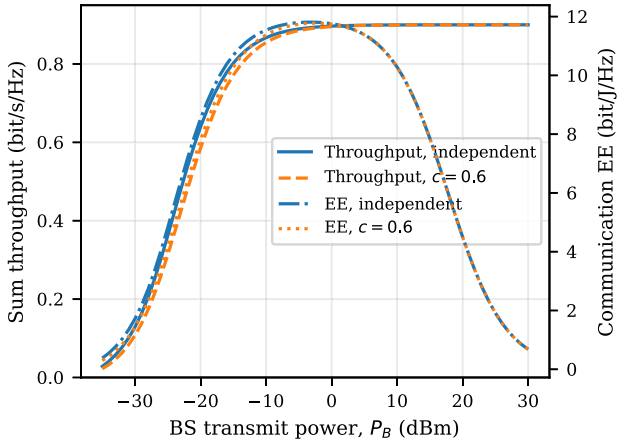



**Fig. 7.** Delay-limited sum throughput and phase-aware external-source communication energy efficiency computed from the approximate outage probabilities.

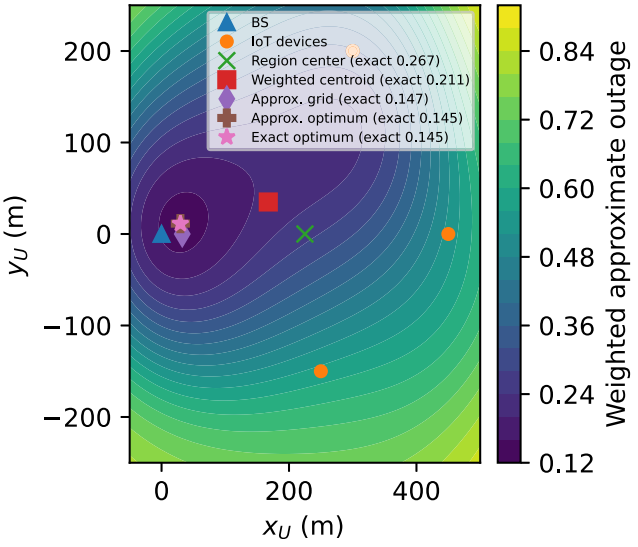



**Fig. 8.** Approximate weighted-outage surface with geometric benchmarks, approximate solutions, and the exact variable-gain optimum. Legend values are exact objectives.

### 4.7. Throughput and communication energy efficiency

Fig. 7 computes both metrics from the approximate outage probabilities. Here, $\Omega_{BU} = \Omega_k = 10^{-3}$, the noise power is −90 dBm, $\xi_B = 2.5$, and the phase-aware circuit powers are listed in Table 1. The independent-port sum throughput increases from 0.129 bit/s/Hz at −30 dBm to 0.639 bit/s/Hz at −20 dBm and approaches the rate ceiling of 0.9 bit/s/Hz at high power. Correlation mainly affects the low- and moderate-power ranges. The communication energy efficiency is unimodal, with maxima of approximately 11.81 bit/J/Hz at −3 dBm for independent ports and 11.78 bit/J/Hz at −2 dBm for correlated ports. Beyond these points, throughput is nearly saturated while the external power consumption continues to increase.

### 4.8. Approximate optimization with exact placement validation

Fig. 8 shows $\mathcal{J}^{\mathrm{ap}}$ for $P_B = 25$ dBm and $\boldsymbol{\omega} = [0.2, 0.3, 0.5]$. The region center and bounded weighted centroid have exact objectives 0.26675 and 0.21133, respectively. The 21 × 19 approximate grid gives (32.5, 0) m with exact objective 0.14743. Approximate refinement gives (29.593, 11.327) m, whereas exact grid-plus-refinement gives (29.593, 11.327) m to the displayed precision; both have exact objective 0.14549. Thus, in this representative state, the approximate optimizer is also exact-objective near-optimal, but this agreement is demonstrated numerically rather than assumed.

**Table 4**
Exact placement sensitivity and surrogate gap.

| $H$ (m) | $\nu_{Uk}$ | Exact $(x_{UAV}, y_{UAV})$ (m) | $\mathcal{J}^{\mathrm{ex}}$ | Gap (%) |
|---|---|---|---|---|
| 70 | 2.6 | (13.81, 5.32) | 0.07083 | $7.4 \times 10^{-6}$ |
| 100 | 2.2 | (24.02, 9.52) | 0.01508 | $<10^{-8}$ |
| 100 | 2.6 | (29.59, 11.33) | 0.14549 | $<10^{-8}$ |
| 100 | 3.0 | (36.25, 11.05) | 0.69432 | $<10^{-8}$ |
| 150 | 2.6 | (77.14, 29.02) | 0.30371 | $<10^{-8}$ |

Table 4 changes the altitude and second-hop path-loss exponent while retaining the same horizontal user geometry. The exact optimum moves toward the BS as the first hop becomes more influential and toward the users as the second-hop attenuation increases. Across all five cases, evaluating the approximate optimizer with the exact objective gives a gap below $7.4 \times 10^{-6}\%$, showing that the close agreement in Fig. 8 is not confined to one altitude.

### 4.9. Data-driven placement with exact test objective

The dataset contains 600 training, 100 validation, and 200 test states. The varied quantities are exactly those in (77). Candidate neighbor counts $L \in \{3, 5, 9, 15, 25\}$ are compared on the validation set,

**Table 5**
Learning Initializers with identical local refinement.

| Method | RMSE (m) | Mean gap (%) | 95th gap (%) | Online (ms) |
|---|---|---|---|---|
| KNN + local | 67.67 | 0.640 | 0.692 | 3.34 |
| Random forest + local | 71.52 | 0.901 | 0.293 | 40.53 |
| MLP + local | 43.51 | 0.115 | 0.237 | 3.57 |

**Table 6**
Test-set placement evaluated with the exact objective.

| Method | RMSE (m) | Mean gap (%) | 95th gap (%) | Time (ms) |
|---|---|---|---|---|
| Unweighted centroid | 171.43 | 57.64 | 190.05 | 0.24 |
| Weighted centroid | 123.88 | 40.29 | 124.66 | 0.23 |
| Coarse approx. grid | 25.15 | 2.95 | 7.11 | 0.30 |
| Data-driven local | 67.67 | 0.64 | 0.69 | 3.45 |
| Approx. optimization | 0.06 | $8.7\times10^{-6}$ | $4.5\times10^{-8}$ | 25.61 |
| Exact optimization | 0 | 0 | 0 | 23.65 |

which selects $L = 9$. Approximate labels are generated by a $21 \times 19$ grid followed by bounded refinement. Exact test references are generated independently from (34).

For a test coordinate $\hat{q}_U$, define the exact-objective gap

$$\epsilon_{\mathcal{J}}^{\mathrm{ex}} = 100\frac{\mathcal{J}^{\mathrm{ex}}(\hat{q}_U) - \mathcal{J}^{\mathrm{ex}}(q_{UAV}^{\mathrm{ex},\star})}{\max\{\mathcal{J}^{\mathrm{ex}}(q_{UAV}^{\mathrm{ex},\star}), 10^{-10}\}}. \tag{79}$$

Table 6 and Fig. 9 show that the data-driven local method attains a mean exact gap of 0.64%, a median of 0.0015%, and a 95th-percentile gap of 0.69%. A nonparametric bootstrap over the 200 test states gives a 95% confidence interval of $[0.19, 1.25]\%$ for the mean gap. Across 20 bootstrap resamples of the training set, the mean exact gap ranges from 0.23% to 0.95%, while the 95th percentile ranges from 0.17% to 3.77%. The coarse approximate grid has a 95th-percentile gap of 7.11%. Its coordinate RMSE is lower than that of the data-driven method, illustrating that coordinate error can be misleading when the outage surface contains broad near-optimal regions. The full approximate optimizer is almost indistinguishable from the exact optimizer on these test states, with a mean exact gap below $10^{-5}\%$.

Reference timings were obtained with the supplied deterministic Python 3.13 script on five virtual AMD EPYC 9V74 CPU cores and are platform-dependent. The data-driven method is slower than a coarse grid but uses substantially less time than the full approximate or exact grid-plus-refinement solvers while providing a markedly smaller exact-objective gap. A separate 100-state stress test expands the user-coordinate, power, altitude, and splitting-ratio ranges beyond the training hyperrectangle. Its median and 95th-percentile gaps are 0.0015% and 0.175%, but the 99th percentile rises to 26.68% and the maximum to 28.81%. The method should therefore be retrained or backed by the full optimizer when the state is outside its documented training range.

To determine whether the simple initializer is justified, Table 5 compares it with a 300-tree random forest and a two-hidden-layer multilayer perceptron (MLP). Every predictor uses the same 600/100/200 split, the same standardized state vector, the same training labels, the same $5 \times 5$ local search, and the same exact-objective test evaluation. The MLP achieves the smallest mean gap, 0.115%, and the lowest coordinate RMSE, whereas KNN retains comparable online time without offline iterative training. The random forest has a lower 95th-percentile gap than KNN but a larger mean gap and substantially longer online evaluation in this implementation. We therefore present KNN as a transparent low-data initializer, not as a universally superior learning model; the MLP is the stronger accuracy benchmark when training and model maintenance are acceptable.

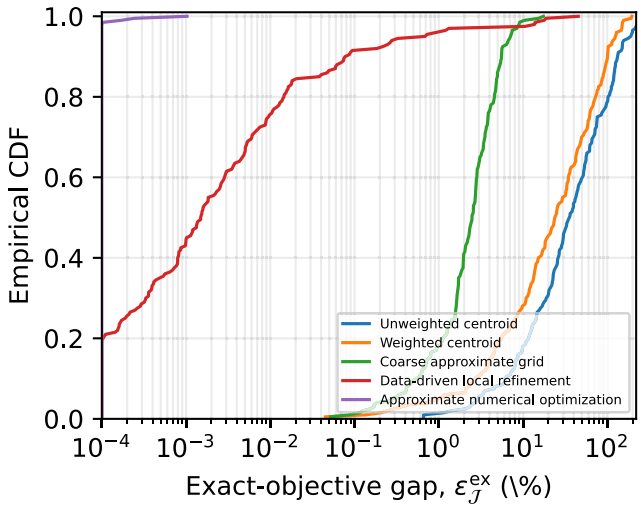



**Fig. 9.** Empirical CDF of the exact variable-gain weighted-outage gap over 200 unseen test states.

### 4.10. Direct benchmark gain relative to a conventional single-port receiver

To make the benefit of FAS reception explicit, Fig. 10 reports the outage-improvement factor relative to the conventional single-port UAV–NOMA–SWIPT receiver. The benchmark metric is defined as

$$\mathcal{G}_{\mathrm{out}}(\bar{\gamma}) = \frac{P_{\mathrm{out}}^{N=1}(\bar{\gamma})}{P_{\mathrm{out}}^{\mathrm{scheme}}(\bar{\gamma})}, \tag{80}$$

so that $\mathcal{G}_{\mathrm{out}} > 1$ directly quantifies the reliability advantage over the fixed-antenna baseline. The same parameters and approximate outage expressions used in Fig. 3 are retained; hence, this comparison introduces no additional modeling assumptions. To add a classical access benchmark without changing the SWIPT relay model, the figure also includes a UAV–OMA–FAS reference with the same FAS parameters $N = 8$ and $c = 0.6$. Under equal user-time allocation among the $K$ users, the corresponding end-to-end outage threshold becomes $\tau_k^{\mathrm{OMA}} = 2^{2\,KR_k} - 1$. At 30 dB, the proposed correlated FAS configuration with $N = 8$ and $c = 0.6$ provides an outage-improvement factor of approximately 5.01, while the ideal independent-port case reaches 6.09. Even under strong dependence, $c = 0.9$, the corresponding factor remains 2.84, whereas the UAV–OMA–FAS benchmark achieves about 4.49. At 40 dB, these factors increase to approximately 7.21, 8.77, 3.91, and 6.39, respectively. The comparison therefore shows that the proposed FAS-assisted NOMA receiver preserves a substantial reliability advantage over conventional single-port reception and also outperforms the UAV–OMA–FAS benchmark for the tested user under the same SWIPT relay model, while the independent-port curve serves as an ideal upper benchmark for the port-selection gain.

## 5. Conclusion

This paper developed exact and approximate outage analyses for a SWIPT-powered variable-gain UAV AF relay serving NOMA users equipped with fluid antennas. The exact layer-decoding conditions produced a one-dimensional outage integral for arbitrary selected-port statistics, while the relay-input-SNR approximation yielded tractable correlated-port integrals and an independent-port closed form. The diversity behavior and the distinct single-port logarithmic case were established. Spatial dependence was modeled through a Gaussian copula calibrated to physical power-gain correlation and validated against complex-channel samples. For deployment, a bounded weighted-centroid benchmark and an exact-validated learned initialization were

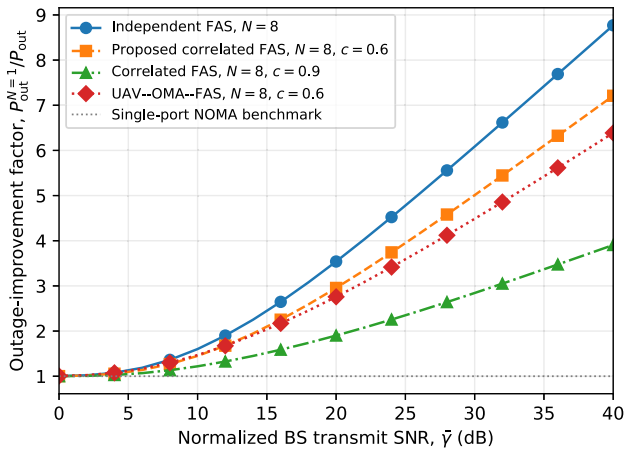



**Fig. 10.** Outage-improvement factor relative to the conventional single-port UAV–NOMA–SWIPT receiver. The additional UAV–OMA–FAS curve uses equal user-time allocation with the same SWIPT relay and FAS parameters. Values above unity indicate a reliability advantage over the $N = 1$ benchmark.

developed. Controlled robustness tests showed that Rician LoS components reduce deep-fade outage, whereas nonlinear harvesting, aged port-selection CSI, and residual SIC can materially degrade the ideal benchmark. Instantaneous order adaptation improved reliability in the tested rank-crossing scenario, confirming that the predetermined service order is a policy assumption rather than a dynamic optimum. Comparison with random-forest and MLP initializers showed that the MLP offers the best average placement accuracy, while KNN remains a transparent low-data option with comparable online time. The closed-form results remain specific to the baseline assumptions; joint analytical treatment of Rician correlated ports, nonlinear EH, imperfect estimation/cancellation, multi-antenna beamforming, and propulsion-aware three-dimensional deployment remains open.

## CRediT authorship contribution statement

**Khalid Yahya:** Writing – original draft, Validation, Software, Project administration, Methodology, Formal analysis, Conceptualization. **Mahmoud Aldababsa:** Writing – original draft, Validation, Supervision, Software, Resources, Investigation, Formal analysis, Conceptualization. **Hamidullah Riaz:** Writing – review & editing, Visualization, Funding acquisition.

## Declaration of competing interest

The authors declare that they have no known competing financial interests or personal relationships that could have appeared to influence the work reported in this paper.

## Data availability

Data will be made available on request.

## References

[1] Chen X, Ng DWK, Yu W, Larsson EG, Al-Dhahir N, Schober R. Massive access for 5G and beyond. IEEE J Sel Areas Commun 2021;39(3):615–37. http://dx.doi.org/10.1109/JSAC.2020.3019724.

[2] Li B, Fei Z, Zhang Y. UAV communications for 5G and beyond: Recent advances and future trends. IEEE Internet Things J 2019;6(2):2241–63. http://dx.doi.org/10.1109/JIOT.2018.2887086.

[3] Mozaffari M, Saad W, Bennis M, Nam Y-H, Debbah M. A tutorial on UAVs for wireless networks: Applications, challenges, and open problems. IEEE Commun Surv & Tutorials 2019;21(3):2334–60. http://dx.doi.org/10.1109/COMST.2019.2902862, thirdquarter.

[4] Wu Q, et al. A comprehensive overview on 5G-and-beyond networks with UAVs: From communications to sensing and intelligence. IEEE J Sel Areas Commun 2021;39(10):2912–45. http://dx.doi.org/10.1109/JSAC.2021.3088681.

[5] Zeng Y, Xu J, Zhang R. Energy minimization for wireless communication with rotary-wing UAV. IEEE Trans Wirel Commun 2019;18(4):2329–45. http://dx.doi.org/10.1109/TWC.2019.2902559.

[6] Kim YH, Chowdhury IA, Song I. Design and analysis of UAV-assisted relaying with simultaneous wireless information and power transfer. IEEE Access 2020;8:27874–86. http://dx.doi.org/10.1109/ACCESS.2020.2971692.

[7] Liu Y, Qin Z, Elkashlan M, Ding Z, Nallanathan A, Hanzo L. Nonorthogonal multiple access for 5G and beyond. Proc IEEE 2017;105(12):2347–81. http://dx.doi.org/10.1109/JPROC.2017.2768666.

[8] Aldababsa M, Mwais A Abu, Obaid M. Performance of STAR-RIS assisted NOMA networks in nakagami-*m* fading channels. AEU–International J Electron Commun 2023;166:154685.

[9] Aldababsa M, Kucur O. BER performance of NOMA network with majority-based JTRAS scheme under practical impairments. AEU–International J Electron Commun 2021;129:153523.

[10] New WK, et al. Fluid antenna systems: Redefining reconfigurable wireless communications. IEEE J Sel Areas Commun 2026;44:1013–44. http://dx.doi.org/10.1109/JSAC.2025.3632097.

[11] Ramírez-Espinosa P, Morales-Jimenez D, Wong K-K. A new spatial block-correlation model for fluid antenna systems. IEEE Trans Wirel Commun 2024;23(11):15829–43. http://dx.doi.org/10.1109/TWC.2024.3434509.

[12] Hoang TM, Nguyen BC, Dung LT, Kim T. Outage performance of multi-antenna mobile UAV-assisted NOMA relay systems over nakagami-m fading channels. IEEE Access 2020;8:215033–43. http://dx.doi.org/10.1109/ACCESS.2020.3041311.

[13] Yin S, Zhao Y, Li L, Yu FR. UAV-assisted cooperative communications with power-splitting information and power transfer. IEEE Trans Green Commun Netw 2019;3(4):1044–57. http://dx.doi.org/10.1109/TGCN.2019.2926131.

[14] Perera TD Ponnimbaduge, Jayakody DNK, Garg S, Kumar N, Cheng L. Wireless-powered UAV assisted communication system in nakagami-m fading channels. In: 2020 IEEE 17th annual consumer communications & networking conference. CCNC, Las Vegas, NV, USA; 2020, p. 1–6. http://dx.doi.org/10.1109/CCNC46108.2020.9045123.

[15] Wang W, et al. Energy-constrained UAV-assisted secure communications with position optimization and cooperative jamming. IEEE Trans Commun 2020;68(7):4476–89. http://dx.doi.org/10.1109/TCOMM.2020.2989462.

[16] Mamaghani MT, Hong Y. Improving PHY-security of UAV-enabled transmission with wireless energy harvesting: Robust trajectory design and communications resource allocation. IEEE Trans Veh Technol 2020;69(8):8586–600. http://dx.doi.org/10.1109/TVT.2020.2998060.

[17] Do D-T, Le A-T, Liu Y, Jamalipour A. User grouping and energy harvesting in UAV-NOMA system with AF/DF relaying. IEEE Trans Veh Technol 2021;70(11):11855–68. http://dx.doi.org/10.1109/TVT.2021.3116101.

[18] Thapliyal S, Pandey R, Charan C. Energy-harvesting-enabled UAV relay-assisted NOMA network under finite blocklength. IEEE Internet Things J 2024;11(13):23255–67. http://dx.doi.org/10.1109/JIOT.2024.3378981.

[19] Boshkovska E, Ng DWK, Zlatanov N, Schober R. Practical non-linear energy harvesting model and resource allocation for SWIPT systems. IEEE Commun Lett 2015;19(12):2082–5. http://dx.doi.org/10.1109/LCOMM.2015.2478460.

[20] Tlebaldiyeva L, Nauryzbayev G, Arzykulov S, Eltawil A, Tsiftsis T. Enhancing QoS through fluid antenna systems over correlated nakagami-m fading channels. In: 2022 IEEE Wireless Communications and Networking Conference. WCNC, Austin, TX, USA; 2022, p. 78–83. http://dx.doi.org/10.1109/WCNC51071.2022.9771633.

[21] Xu H, Wong K-K, New WK, Tong K-F, Zhang Y, Chae C-B. Revisiting outage probability analysis for two-user fluid antenna multiple access system. IEEE Trans Wirel Commun 2024;23(8):9534–48. http://dx.doi.org/10.1109/TWC.2024.3363499.

[22] Abdou SBS, New WK, Leow CY, Won S, Wong K-K, Ding Z. Sum-rate maximization for UAV relay-aided fluid antenna system with NOMA. In: 2024 IEEE 7th international symposium on telecommunication technologies. ISTT, Langkawi Island, Malaysia; 2024, p. 53–8. http://dx.doi.org/10.1109/ISTT63363.2024.10750660.

[23] Ghadi F Rostami, Kaveh M, Hernando-Gallego F, D. Martín K-K Wong, Chae C-B. UAV-relay assisted RSMA fluid antenna system: Outage probability analysis. IEEE Wirel Commun Lett 2025;14(9):2907–11. http://dx.doi.org/10.1109/LWC.2025.3582753.

[24] Xu R, et al. On performance of fluid antenna relay (FAR)-assisted AAV-NOMA wireless network. In: 2026 IEEE wireless communications and networking conference workshops. WCNCW, KUALA LUMPUR, Malaysia; 2026, p. 1–6. http://dx.doi.org/10.1109/WCNCW67598.2026.11555079.